applied sciences

MDPI

Article

Application of Unconstrained Cobalt and Aluminium Metal Powders in the Alloying of Carbon Steel in Submerged Arc Welding: Thermodynamic Analysis of Gas Reactions

Theresa Coetsee * and Frederik De Bruin

Department of Materials Science and Metallurgical Engineering, University of Pretoria, Pretoria 0002, South Africa
* Correspondence: theresa.coetsee@up.ac.za

Abstract: The application of cobalt and aluminium powders in unconstrained format, not as metal powder in tubular wire nor as pre-alloyed powder, is used in this work to simplify weld metal alloying. The objective of this study is to demonstrate the application of unconstrained cobalt and aluminium powders in Submerged Arc Welding SAW to alloy the weld metal and to control the weld metal oxygen content. Aluminium powder is used to control the oxygen potential at the weld pool-slag interface in order to prevent oxidation of cobalt. The results presented here show that with the addition of Aluminium powder, 70% yield of Cobalt was achieved from the cobalt powder to the weld metal. The carbon steel base-plate material and weld wire materials combination were alloyed to 5.3% Co and 4.2% Al, whilst controlling the weld metal total oxygen content to 230 ppm. Thermodynamic analysis is applied to investigate the possible chemical interaction reactions between Co and Al compounds, as well as the role of the reactions on Co yield to the weld pool. The application of unconstrained metal powders ensures productivity gains in the overall SAW process because the time consuming and expensive manufacturing of alloyed wire and alloyed powder are eliminated.

Keywords: pyrometallurgy; powder; cobalt; oxygen control; aluminium; welding

Citation: Coetsee, T.; De Bruin, F. Application of Unconstrained Cobalt and Aluminium Metal Powders in the Alloying of Carbon Steel in Submerged Arc Welding: Thermodynamic Analysis of Gas Reactions. *Appl. Sci.* **2022**, *12*, 8472. https://doi.org/10.3390/app12178472

Academic Editor: Chiara Soffritti

Received: 12 July 2022
Accepted: 22 August 2022
Published: 25 August 2022

1. Introduction

Submerged arc welding (SAW) is mainly used in heavy engineering industries as a method of joining thick steel plates at high productivity rates due to its intensive energy input into the weld area. Examples of SAW application in heavy engineering include the construction of large ships and offshore structures [1]. SAW is also used as high productivity method in the application of expensive, specialist cladding materials onto substrate materials of low cost or inferior properties. For example, the application of hardfacing layers onto softer steel substrate, and the cladding of reactor vessel interior surfaces with corrosion resistant materials [2]. SAW process requirements may differ somewhat depending on the application; for example, considerable weld metal penetration is required for quality weld joints compared to low weld metal penetration and high surface spread for cladding applications. However, the process fundamentals of SAW remain the same, irrespective of these application differences.

Flux is involved in several critical tasks essential to the pyrometallurgical reactions in the SAW process. One such essential function is the control of total ppm O in the weld metal. The total weld metal oxygen content determines the weld metal impact toughness of carbon steel. It was shown that high impact toughness is maintained in the weld metal within the total oxygen content band of 200 ppm to 500 ppm O [3]. The initial level of total ppm O entering the weld pool via molten weld wire droplets was measured at 2000–3000 ppm O [4,5]. It has been experimentally shown that the dissociation of oxides in the molten flux (slag) in the arc cavity is the only source of this 2000–3000 ppm O in the SAW process [6]. It can be reasonably expected that the arc plasma stability of oxides

should follow the order of thermodynamic stability, due to the high temperatures in the arc cavity. However, experiments have shown that the arc plasma stability order of oxides does not follow the thermodynamic stability order of oxides. The stability of oxides in the arc plasma was investigated during welding tests made under an argon gas atmosphere. Binary oxide–CaF_2 flux mixtures were used as flux. In separate welding tests, for each binary oxide–CaF_2 flux, the order of arc plasma stability of oxides was determined from the extent of total ppm O increase in the weld metal. The least stable oxide formed the highest total ppm O in the resultant weld metal. The work concluded that the order of oxides from the most stable to least stable was as follows: CaO, K_2O, Na_2O, TiO_2, Al_2O_3, MgO, SiO_2, and MnO [7]. Consequently, the weld metal total ppm O can be lowered by adding more CaF_2 into the flux to dilute the quantity of low stability oxides in the molten flux(slag). Empirically determined measurements were used to construct the widely employed flux composition basicity index, the BI, as expressed in Equation (1). The general guideline is to ensure that the flux BI is larger than 1.5, to limit the weld metal hydrogen and weld metal total oxygen content (ppm O) to acceptable levels [8,9].

$$BI = \frac{\%CaF_2 + \%CaO + \%MgO + \%BaO + \%SrO + \%Na_2O + \%K_2O + \%Li_2O + 0.5(\%MnO + \%FeO)}{\%SiO_2 + 0.5(\%Al_2O_3 + \%TiO_2 + \%ZrO_2)} \quad (1)$$

From the above discussion, it is clear that process chemistry is very important in controlling the carbon steel weld metal total oxygen content, from this initial high level of 2000–3000 ppm, to within the acceptable ppm O range of 200–500 ppm. In addition to the formulation of fluxes for oxygen and hydrogen control, flux chemistry is formulated to achieve targeted element transfer levels from the slag to the weld metal [10–14]. Therefore, any changes to the formulation and application of SAW consumables will influence the SAW chemical reactions and should be tested to quantify the effects on process chemistry. In this work, aluminium powder is applied to control the total ppm O, as in our previous works [15–20]. A combination of cobalt powder with aluminium powder is applied to quantify yield numbers and test the process chemistry of this combination of metal powders. Because cobalt has a low affinity for oxygen, it is typically added into the SAW weld pool from alloyed weld wire. Cobalt is often used in hardfacing applications as the well-known cobalt–chromium based alloy, Stellite [2,21]. It is known that the vaporisation extent of nickel and cobalt is higher in laser cladding than in arc welding methods, although the metal vapours are quickly oxidised to nickel oxide and cobalt oxide in the atmosphere [22]. Manual oxyacetylene welding can also be used in cladding, with consumables in the form of alloy rod or alloy powder [2,21]. Cobalt is added to high temperature applications steel (9% Cr) at 3% Co to improve creep resistance in newly developed steel grades for ultra-supercritical (USC) power generation plant applications [23,24].

Hardfacing alloys may be applied in SAW as pre-alloyed metal powders [25]. Similar to nickel-containing pre-alloyed powders, the application in SAW of iron-based cobalt-containing pre-alloyed powders at up to 40% Co can provide several advantages [25]. The use of pre-alloyed powders in SAW allows for better control of the required chemistry in coating applications, because the pre-alloyed powder chemistry can be tailored to the required chemistry for the specific application [25]. In addition, the use of pre-alloyed powders to form the cladding alloy, as compared to alloy formation via the weld wire, limits weld metal dilution. Dilution from the iron contained in the weld wire is negated, and dilution from the substrate steel is limited because the weld pool is cooled due to the melting of the added powders. Overall deposition productivity is also improved due to the application of metal powders [25]. In the application of pre-alloyed Ni-containing powders, containing 27–29% Cr, 5–8% Ni, 2–4% Mo in iron alloy matrix, the nickel yield values ranged from 57 to 78% [25]. Although the same patent referred to the application of Co-containing pre-alloyed powders with up to 40% Co, no yield data was mentioned.

Because Ni and Co have similar oxygen affinity, melting and boiling points, and vapor pressures vs. temperature, it may be expected that cobalt's yield to the weld metal is similar to that of nickel. However, cobalt yield information seems to be limited or has often been

assumed to be 100%. Since cobalt is expensive at $US 27/lb currently, and price increases are expected due to cobalt demand associated with Li-ion battery manufacture for electric cars, it is important to maximise Co yield to the weld metal [26,27]. Therefore, investigation of cobalt's chemical behaviour in SAW is of importance, irrespective of its application in cladding or joining operations.

Although aluminium is not typically added in large quantities to steel, recent developments of low density/high-entropy steels and low density stainless steels require high quantities of aluminium in their formulations [28,29]. Therefore, it is expected that combinations of alloying elements with aluminium will become increasingly important in expanding the application of SAW to these newer steel grades.

Manufacturing weld wires of specific compositions is expensive and time consuming. Furthermore, available weld-wire compositions are limited and cannot match all desired alloy compositions. Closer matched alloying of the weld metal may be better accomplished if metal powder is applied to the welding process to achieve the desired weld metal composition [25]. Pre-alloyed powder manufacturing is also time consuming, and suffers from limits in matching capabilities; a better cost alternative is the application of unconstrained metal powders in SAW.

A limited number of published studies are available on the application of unconstrained (not fluxed cored wire or metal cored wire) metal powders for alloying purposes in SAW. In particular, the behaviour of cobalt when used as alloying powder is not clear, although it has been qualitatively reported as equally vapour-forming to nickel in the same welding process [22]. The objective of the current study is to demonstrate the application of unconstrained cobalt and aluminium powders in SAW, to alloy the weld metal and control the weld metal oxygen content. The SAW process chemical interaction of Al and Co metal powders with welding flux has not been specifically discussed in the published literature. Therefore, the secondary objective of this work is to apply thermodynamic analysis to elucidate the chemical behaviour of Co and Al metal powders in the SAW process.

2. Materials and Methods

2.1. Welding Tests

SAW runs were made as bead-on-plate weld runs, to investigate the chemical interaction of Al and Co metal powders in SAW. Aluminium metal powder was added to control the partial pressure of oxygen at the weld-pool–slag interface, which determined the weld pool oxygen content [15–20]. A separate weld run was made without addition of any metal powder, and used as the base case, for comparison to the effects of the added metal powders. The bead-on-plate welding test runs were made onto carbon steel plates of dimensions: 350 mm length, 12 mm plate thickness, 300 mm plate width. Weld heat input was 2.0 kJ/mm (500 A, 28 V, 42 cm/minute) welded DCEP (direct current electrode positive). The weld wire was 3.2 mm diameter. The SAW welding equipment consisted of a Lincoln Electric IDEALARC® DC-600 power source linked to a Lincoln Electric NA-3N solid-state automatic wire feeder. The feed ratio of Al to Co was one to one, at 7 g Al and 7 g Co. The steel base plate material was not pre-heated prior to welding.

2.2. Materials and Analyses

Structural steel of grade S355J2+N as specified by EN 10025-2 was used as base plate material, because it is readily available carbon steel. The major element analysis of the weld wire presented in Table 1 is the supplier's specification sheet analysis (Afrox Ltd., Johannesburg, South Africa). The base-plate steel was analysed by optical emission spectroscopy (OES), SPECTRO Analytical Instruments GmbH, model SpectroMax XF, 2018. The total oxygen content in the base plate and weld wire was analysed by combustion method. Table 1 summarises the weld wire and base plate analyses.

Table 1. Base plate and weld wire compositions (mass%).

	%C	%Si	%Mn	%O	%Al	%P	%S	%Ti	%Cu	%Cr	Balance
Plate	0.120	0.155	1.340	0.0007	0.067	0.019	0.007	0.005	0.030	0.160	Fe
Wire	0.110	0.137	0.990	0.0003	0.000	0.009	0.023	0.000	0.140	0.000	Fe

Cross-section samples of the welded plate were cut from the middle position of the weld run. One of these volume samples was analysed for major elements by inductively coupled plasma optical emission spectroscopy (ICP-OES), Thermo Fisher Scientific, Waltham, MA, USA, model iCAP 6000 series, 2008. The second volume sample was used for total oxygen and carbon analysis, by combustion method. The third weld metal cross-section sample was analysed by SEM (scanning electron microscope) after polishing to a mirror finish and etching with 2% Nital solution to reveal the weld metal boundary on the base plate. The SEM equipment assembly consisted of a Zeiss (Oberkochen, Germany) crossbeam 540 FEG (field emission gun) SEM with EDS (energy dispersive spectrometer), Oxford Aztec system with X-Max 80 detector (2015).

A commercial agglomerated flux was selected for use in the welding tests following initial testing of different fluxes [30]. The main selection consideration for the flux was the thermodynamic stability of the flux constituents in the presence of aluminium metal. This flux can be classified as an aluminate basic flux (Basicity Index (BI) = 1.4) and its chemistry and mineralogy have been extensively investigated previously [30]. It has a 0.2–1.6 mm agglomerate particle size. The bulk chemistry of the flux is shown in Table 2. Metal powders of pure Al (99.7% Al and—1 mm) and pure Co (99.9% Co and—0.15 mm) were sourced from Sigma-Aldrich.

Table 2. Flux bulk chemical composition (mass%).

MnO	CaO	SiO_2	Al_2O_3	CaF_2	MgO	FeO	TiO_2	Na_2O	K_2O
6.8	0.1	19.6	24.9	17.9	22.2	2.4	1.0	1.6	0.2

2.3. Thermochemical Calculations

A thermodynamic analysis of gas phase reactions was carried out using FactSage 7.3 thermochemical software [31]. Firstly, a simplified approach was taken to investigate the possibility of fluoride-based reactions of the main flux and metal powder elements, by comparison of the standard Gibbs free energy values for these reactions. The Gibbs free energy values were calculated in the reaction module of FactSage. Secondly, the Equilib module in FactSage 7.3 was employed to calculate the gas–slag-metal-powder equilibrium between the molten flux (slag) and the alloy powders with different aluminium input levels. The thermodynamically predicted gas phase species and the cobalt powder loss to the gas phase were used to interpret the gas phase reaction changes due to the addition of cobalt and aluminium in the SAW process. The FToxid, FSstel and FactPS databases were selected, with the inclusion of plasma species [31].

3. Results

3.1. Chemical Analyses

The weld metal compositions are summarised in Table 3. The weld metals from the two test runs are compared: one without metal powder addition (BC) and one with metal powder addition (MP7). Confirmation of the alloying effect of the cobalt and aluminium metal powders in the MP7 weld metal was affirmed by the EDS analyses shown in Table 4. The area selected for EDS analyses shown in Figure 1 is positioned at the geometric centre of the weld metal cross-section. Although the SEM-EDS equipment cannot analyse %C and %O, the alloying element levels from SEM shown in Table 4 support the detailed bulk chemistry analysis.

Table 3. Weld metal compositions (mass%).

	%C	%Si	%Mn	%O	%Al	%P	%S	%Co	%Cr	%Fe
Base case	0.110	0.260	1.300	0.0499	0.032	0.022	0.011	0.006	0.110	98.03
MP7	0.105	0.410	1.723	0.0230	4.200	0.023	0.011	5.340	0.163	87.71

Table 4. SEM-EDS analyses of marked areas in the weld metal as indicated in Figure 1 (mass%).

	%Si	%Mn	%Al	%Co	%Fe
a	0.93	1.75	3.72	5.47	88.1
b	0.80	1.70	3.90	5.50	88.1
c	0.90	1.70	3.70	5.40	88.3

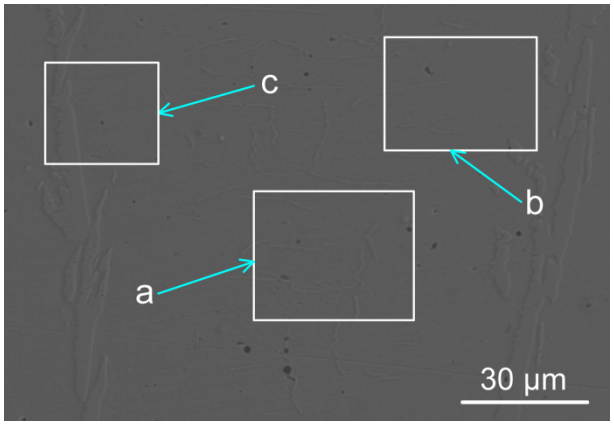

Figure 1. SEM micrograph of weld metal with analysed areas as marked (a–c): (×2000).

Table 3 displays the bulk chemical analyses of the BC and MP7 weld metals. It is clear that the %Mn and %Si increased in the MP7 weld metal. This effect was due to the aluminothermic reduction of SiO_2 and MnO from the flux into the weld metal, as displayed in Equations (2) and (3). It is notable that the weld metal total ppm O was significantly lower in MP7 compared with the BC weld metal, at 230 ppm O vs 499 ppm O, respectively. These ppm O values confirm the de-oxidiser role of aluminium at the weld-pool–slag interface [15–20].

As confirmed in previous studies, FeO in slag is formed from excess oxygen transferred from the arc cavity to the weld metal. The FeO was reduced by aluminium powder via reaction (4) to control the oxygen potential at the weld pool-slag interface [23–28]:

$$3(SiO_2) + 4(Al) = 3(Si) + 2(Al_2O_3) \quad \Delta H^{\circ}_{2000^{\circ}C} = -82.1 \text{ kJ/mol Al} \tag{2}$$

$$3(MnO) + 2(Al) = 3(Mn) + (Al_2O_3) \quad \Delta H^{\circ}_{2000^{\circ}C} = -248.4 \text{ kJ/mol Al} \tag{3}$$

$$3(FeO) + 2(Al) = 3(Fe) + (Al_2O_3) \quad \Delta H^{\circ}_{2000^{\circ}C} = -416.5 \text{ kJ/mol Al} \tag{4}$$

( ): liquid.

From the increased %Mn and %Si in the MP7 weld metal, it can be concluded that the contact time between the aluminium powder and the flux in the welding test was sufficient for reactions (2) and (3) to proceed forward significantly. The Al_2O_3 products formed from reactions (2) and (3) were absorbed into the molten flux, as these reactions occurred at the molten flux–weld-pool interface, and the total ppm O was lowered due to the removal of Al_2O_3 from the weld pool [15–20].

3.2. Mass Balance

Mass balance measurements and calculations were required for the quantification of the yields of Co and Al powders to the weld metal. The calculation procedure was as applied previously [15,18–20]. The steel plate mass was recorded before and after welding, and the mass difference quantified the mass of weld wire and metal powder added to the weld metal. The etched cross-section was used to measure the weld metal areas above and below the base plate top surface, using stereoscope software applied to stereoscope images of the weld metal cross-section. The areas of both weld-metal cross-sections are marked in Figure 2: the area between lines A and B is the proportional area above the base-plate's top surface level. This is the proportion of the weld metal contributed by the weld wire and metal powder, namely Area 1. The proportional area between line B and line C is the proportion of the weld metal area contributed by melting of the base plate, namely Area 2. Here, as previously reported, this area proportion is defined as the dilution ratio and named ($\%DR_{(wire+MP)}$) [15,18–20]. The geometric proportions of the weld bead as displayed in Figure 2 were 12.3 mm width and 6.7 mm height. The weld bead's total run length of 260 mm was made as a continuous bead-on-plate weld run.

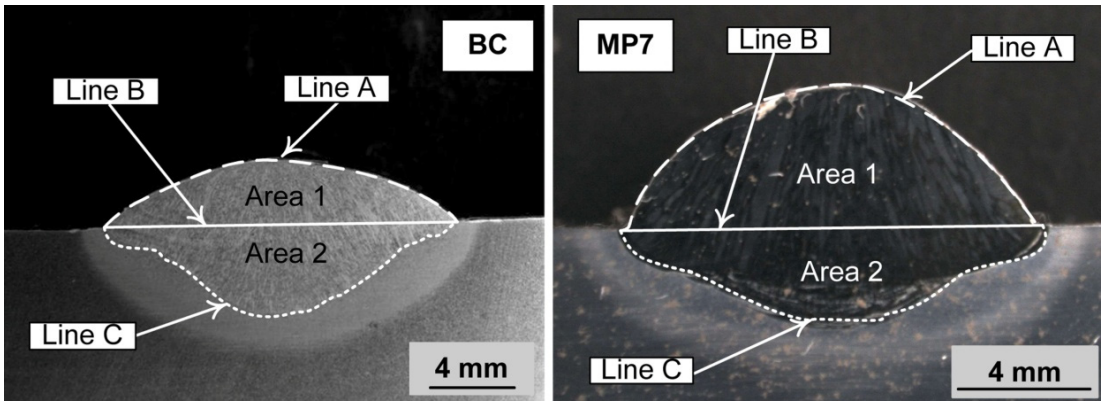

Figure 2. Weld metal cross-section micrographs via stereoscope.

The mass of aluminium and cobalt powders added into the weld metal, respectively, were calculated by Equations (5)–(7). The weld metal composition in Table 3 was used as input for Equation (7). The expressions in Equations (5)–(7) illustrate the calculation sequence for aluminium:

$$\%DR_{(wire+MP)} = \left(\frac{A_{(wire+MP)}}{A_{(wire+MP)} + A_{BP}}\right) * 100 = \left(\frac{Area1}{Area1 + Area2}\right) * 100 \quad (5)$$

$$m_{WM} = (m_{wire} + m_{MP}) * \left(\frac{100}{\%DR_{(wire+MP)}}\right) \quad (6)$$

$$(\text{gram Al to WM}) = (m_{WM}) * \left(\frac{\%Al_{WM}}{100}\right) \quad (7)$$

WM = weld metal; MP = metal powder; BP = base plate; Wire = weld wire; m = mass (gram); A = area (mm^2)

Similarly, the calculation for cobalt was made by using %Co in the weld metal, shown in Table 3, as input for Equation (7).

From the gram masses of aluminium and cobalt powder added to the weld metal, as calculated from Equations (5)–(7), the percentage yield of each element to the weld metal was calculated from the initial input mass of 7 g of Al and 7 g of Co. Table 5 summarises the numbers applied in Equations (5)–(7), and the calculation results from Equation (7). The resultant percentage yields for Co and Al were 70% and 55%, respectively.

Table 5. Mass balance numbers for percentage yield calculation.

	Al (g)	Co (g)	Powder (g)	Wire (g)	Base Plate (g)	Weld Metal (g)	$\%DR_{(wire + MP)}$	%Al Yield	%Co Yield
Base Case	0	0	0	33.8	33.8	67.6	50	0	0
MP7	3.9	5.0	8.9	51.1	33.5	93.5	64	55	70

Because reactions (2) and (3) are exothermic reactions, the extent of the heat contributions from these reactions was quantified to determine the possible temperature increase in the weld metal due to this added chemical heat. The added chemical heat values were calculated by first quantifying the mass of manganese and silicon added into the weld metal during these reactions, by using equation (8), as reported previously [15,18–20]. Equation (8) shows the calculation for the mass of Mn added during aluminothermic reduction (M_{Mn}). The inputs for Equation (8) were the weld metal mass (Mwm) and the dilution ratio value ($\%DR_{(wire+MP)}$), from Table 5, for the base case, and the %Mn in the weld metal, from Table 3. The square bracketed terms in Equation (8) represent the calculation of the BC weld metal nominal composition:

$$M_{Mn} = (M_{WM})\left(\frac{\%Mn_{WM}}{100} - \left[\frac{\%DR_{wire}}{100} * \frac{\%Mn_{wire}}{100}\right] - \left[\left(1 - \frac{\%DR_{wire}}{100}\right) * \frac{\%Mn_{BP}}{100}\right]\right) \quad (8)$$

M = mass (gram); M_{WM} = mass Mn (gram); $\%Mn_{WM}$ = %Mn in weld metal; %DRwire = % of weld metal contributed by weld wire in the base case (BC); %Mnwire = %Mn in weld wire; $\%Mn_{BP}$ = %Mn in base plate (BP); WM = weld metal; BP = base plate; Wire = weld wire.

The exothermic heat from reactions (2) and (3) can be calculated from the reaction enthalpy values displayed next to reactions (2) and (3). The simplified translation of the kJ values was made by using the heat capacity of steel (0.460 kJ/kg K) to calculate the expected increase in weld metal temperature from the exothermic heat released in reactions (2) and (3) according to the mass of SiO_2 and MnO reacted, as calculated in Equation (8) and displayed in Table 6. The reaction heat values from the calculations are summarised in Table 6. Although only small quantities of SiO_2 and MnO were involved in reactions (2) and (3), the exothermic heat added into the weld metal was significant as an instantaneous increase of 58 °C in the weld metal temperature was generated. This exothermic heat may contribute to the melting of metal powders for incorporation into the weld pool.

Table 6. Exothermic heat added to the weld pool from reactions (2) and (3).

	SiO_2 (g)	MnO (g)	Al (g)	Reaction (2) (kJ)	Reaction (3) (kJ)	Reactions (2) & (3) (kJ)	Weld metal ΔT (°C)
MP7	0.53	0.67	0.49	−0.96	−1.57	−2.53	58

It has been established that the weld pool solidification time plays an important role in the control of total oxygen content in the weld pool. This effect is due to an increase in the weld pool cooling time, which then in turn provides more time for oxide inclusions to float from the weld pool to the slag–weld-pool interface and be absorbed into the molten slag [32]. The weld pool cooling time, set by the difference between the weld pool liquidus and solidus temperatures, may be different for differing weld-pool chemistries. Figure 3 displays the solidification curves for the BC and MP7 weld-metal chemistries; see Table 3.

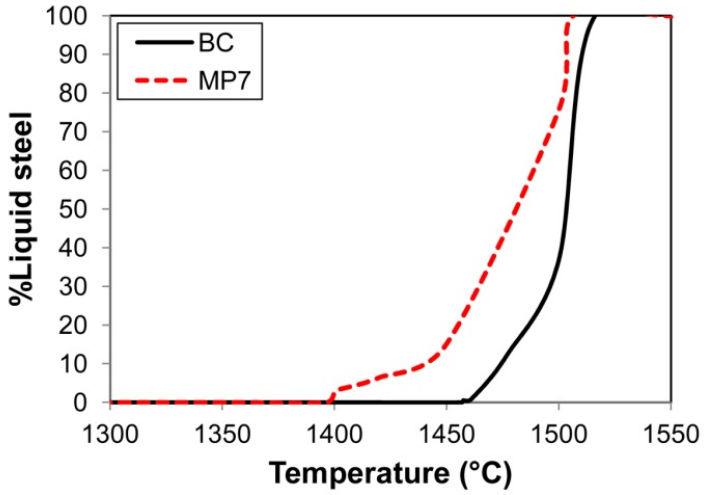

Figure 3. Solidification curves for BC and MP7 weld metal compositions as calculated in FactSage 7.3 [31].

FactSage 7.3 thermochemical software, using the Equilib module and the FToxid and FSstel databases, was used to calculate the solidification curves displayed in Figure 3 [31]. Comparison of these curves confirms that the solidus temperature of MP7 weld metal is lower than the solidus temperature of the base case (BC) weld metal. Consequently, the longer cooling time of the MP7 weld pool, compared with the BC weld pool cooling time, contributed to a lower total ppm O in the MP7 weld metal at 230 ppm O compared with the BC weld metal at 499 ppm O, see Table 3.

4. Discussion

A thermodynamic analysis was applied to elucidate the chemical interaction between cobalt and aluminium, and its effects on cobalt yield to the weld pool. During SAW, a variety of complex reactions take place in the arc cavity, and these reactions may contribute to cobalt loss. For example, some of the cobalt is expected to vaporise, cobalt may react with F_2(g) and/or CaF_2(g) to form CoF_2(g), and cobalt may also oxidise to CoO. As a starting point, simple thermodynamic calculations for typically expected chemical reactions were performed to investigate the relative likelihood of possible reactions involving CoF_2(g) formation, relative to similar reactions for different compounds contained in the flux, metal powders, and steel. The first reactions considered for metal fluoride formation were of the type in Equation (9), with the reactions' standard Gibbs free energy values displayed in Figure 4. The second type of reaction considered for metal fluoride formation were those displayed in Equation (10), with the Gibbs free energy values displayed in Figure 5. The values in Figures 4 and 5 were calculated using FactSage 7.3 thermochemical software [31]. A calculation temperature interval of 1600 °C to 2500 °C was selected to include temperatures applicable to the main reactions in SAW, as identified in previous works, namely 2000 °C as the effective slag–metal equilibrium reaction temperature, 2500 °C at the plasma–weld-pool interface, down to 1600 °C which is close to the liquidus temperature of steel [9,10,33].

$$[\mathrm{Co}] + [\mathrm{F_2}] = [\mathrm{CoF_2}] \tag{9}$$

$$(CoO) + [CaF2] = [CoF2] + <CaO>() : liquid; [] : gas; <> : solid. \tag{10}$$

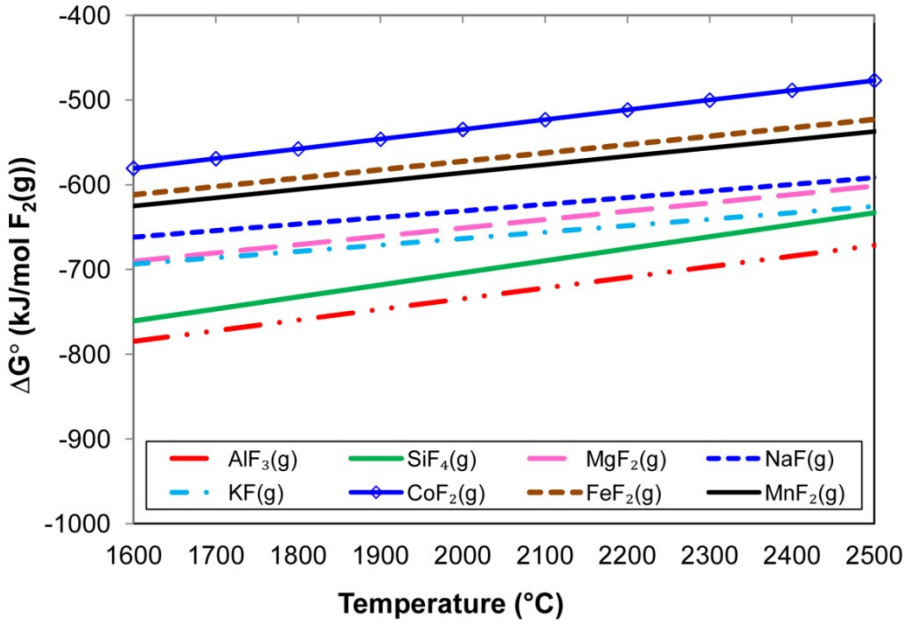

Figure 4. Standard Gibbs free energy for metal vapour and F_2 gas reactions as calculated in FactSage 7.3 [31].

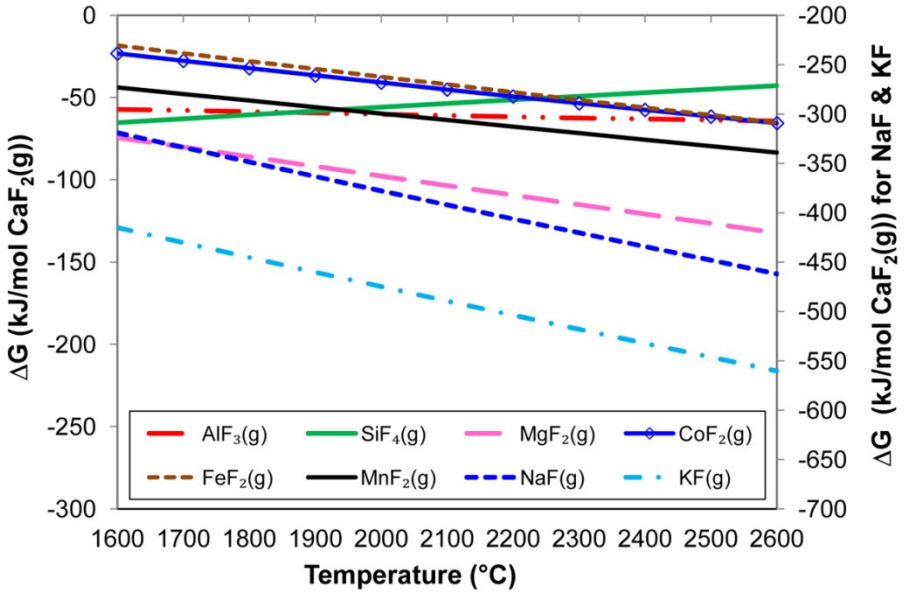

Figure 5. Gibbs free energy for metal oxide and CaF_2 gas reactions as calculated in FactSage 7.3 [31].

The following input values were applied to calculate the standard Gibbs free energy values displayed in Figure 4: 1 atm for each gas, namely metal vapour, F_2(g), and the product metal fluoride gas. The input values applied for the Gibbs free energy value calculations displayed in Figure 5 were: 1 atm CaF_2(g) unit activity for the molten metal oxides, 0.10 atm for the metal fluoride gas formed, and 0.01 activity for the CaO formed from reaction (10). From the standard Gibbs free energy values displayed in Figure 4, the formation of CoF_2(g) was found to be least likely among the metal vapour reactions with F_2(g). However, in comparison to the Gibbs free energy values in Figure 5, all reactions of type (9) were more likely to occur than reactions of type (10). Therefore, the reaction of CoO with CaF_2(g) was less likely than the reaction of Co(g) with F_2(g) to form CoF_2(g). A multitude of reactions are possible at the high temperatures prevailing in the arc cavity,

beyond the simple reactions of types (9) and (10) discussed above, and the following thermochemical simulation calculations were made.

The Equilib module in FactSage 7.3 was used to calculate the gas–slag–metal-powder equilibrium between the molten flux (slag) and the alloy powders. The FToxid, FSstel, and FactPS databases were selected, with the inclusion of plasma species [31]. The flux input composition was that shown in Table 2, and the flux mass input was equal to slag mass measured for the post-weld slag. The cobalt input mass was 7 g as feed into the weld run. The aluminium input mass was varied between zero and the maximum of 6.5 g aluminium, since the mass balance calculations showed that 0.50 g of the 7 g of aluminium input was consumed in reactions (2) and (3). In addition, it is possible that the quantity of aluminium reported in the weld metal did not fully participate in gas-based reactions. Therefore, one scenario was calculated to simulate this possibility of 3.25 g aluminium input. The calculated gas compositions and quantities are summarised in Table 7.

Table 7. Gas composition output from gas–slag–metal powder equilibrium at 2500 °C, calculated in FactSage 7.3 Equilib module [31].

Gram Al	%MgF_2	%MgF	%Mg	%AlF_3	%AlF_2	%AlF	%CaF_2	%NaF	%Na	%Mn	%MnF_2	%Co	%SiO	Mass%Co to Gas
zero	27	5	2	5	3	1	21	12	4	2	2	10	1	10
3.25	7	8	16	1	5	16	7	3	5	9	<0.5	8	9	16
6.50	2	5	25	0.3	3	24	2	1	4	8	<0.5	7	15	23

The calculation speciation results confirmed that increased aluminium added into the arc cavity can maintain the cobalt in the metallic state via lowered gas-phase partial oxygen pressure, resulting in cobalt metal vaporisation rather than formation of CoF_2(g). The gas composition volume% CoF_2(g) values are low at 1%, 0.01%, and 0.002%, as calculated for zero, 3.25, and 6.50 g of added aluminium, respectively. Because somewhat larger gas volumes are formed with aluminium reactions, the cobalt mass balance numbers in the last column in Table 7 indicate that more cobalt is vaporised at higher aluminium additions, even though the %Co in the gas decrease with increased aluminium. The partial oxygen pressure values of the gas phase were calculated as 6.3×10^{-5} atm, 4.0×10^{-7} atm, and 8.5×10^{-8} atm for zero, 3.25, and 6.50 g of aluminium, respectively, illustrating that more effective reducing conditions prevailed in the arc cavity with increased addition of aluminium powder. From the results in Table 7, it appears that CaF_2(g) and MgF_2(g) are replaced by Mg(g), AlF(g), Mn(g), and SiO(g) due to the chemical interactions with added aluminium in the arc cavity. Although this calculation is a simplification of the overall process, the speciation outputs from the calculation are in agreement with the deductions made from the consideration of simplified reactions in Figures 4 and 5. In Figure 4 it can be seen that AlF_3(g) formation from Al is thermodynamically most probable and CoF_2(g) is thermodynamically least probable. This means that the forward reaction (9) for Al and reverse reaction (9) for Co sum to reaction (11), below, so that any CoF_2(g) presnet in the gas phase will be easily transformed to cobalt vapour via the reaction with Al vapour. This reaction is in agreement with the calculated composition of the equilibrium gas phase shown in Table 7, showing cobalt vapour but little CoF_2(g) in the gas, as enumerated in the text above. Although AlF_3(g) is displayed in reaction (11), the same type of reaction is also favoured in the formation of AlF_2(g) and AlF(g) because the standard Gibbs free energies for the formation of these compounds are lower than for formation of AlF_3(g) from Al(g) and F_2(g), as displayed in Figure 6:

$$2[Al] + 3[CoF_2] = 2[AlF_3] + 3[Co] \quad (11)$$

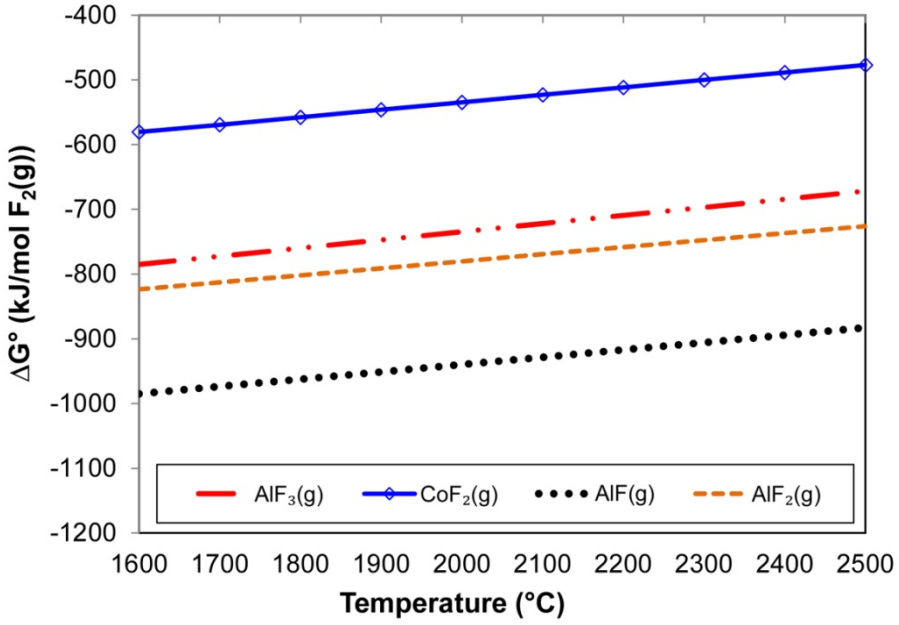

Figure 6. Standard Gibbs free energy for metal vapour and F_2 gas reactions of Al and Co as calculated in FactSage 7.3 [31].

Considering the behaviour of cobalt in the presence of aluminium in the gas-based reactions discussed above, the likely reaction sequence in the SAW process with the use of aluminium and cobalt powders is shown in Figure 7. Reaction steps A to E, as displayed in Figure 7, are as presented in previous works [4–6,33,34]. Reaction steps A to E represent oxygen transfer from the molten flux (slag) to the weld pool. Reaction A corresponds to the same type of reaction as equation (10), for the reaction of Al_2O_3 with CaF_2(g) to form AlF_3(g) and CaO. This reaction has the lowest Gibbs free energy values, as displayed in Figure 4. Previous studies conclusively showed that the initial excessive quantity of oxygen added into the weld pool via the molten weld wire droplets from the arc cavity gas phase may be up to 2000–3000 ppm O [4,5]. The word "excessive" means that the ppm O in the weld pool exceeds the solubility limit of oxygen at the cooling weld-pool temperature once the arc has passed and the weld pool cools from the high arc plasma temperatures, typically 2000 °C to 2500 °C [9,10,33].

This initial excessive oxygen quantity in the metal droplets is due to the decomposition of less stable oxides at the high temperatures prevailing in the arc plasma. Therefore, flux chemistry is used to manage oxygen transfer to the weld metal from the arc plasma [7]. Considering the established hierarchy of oxide stability in the arc plasma, the MnO, SiO_2, MgO, and Al_2O_3 contained in the aluminate basic flux used in this work may all have dissociated in the arc plasma to release oxygen in the arc cavity. This oxygen was then adsorbed onto the molten weld wire droplets for transfer to the molten weld pool via the arc-plasma–weld-pool interface; see reactions A to C in Figure 7 [7].

Previous works have shown that the excessive quantity of oxygen transferred from the arc cavity reacts with the molten steel at the arc-plasma–weld-pool interface to form FeO; see reaction E in Figure 7. This FeO is incorporated into the slag. The correlation of increased FeO in the molten flux with increased weld-metal ppm O has been well illustrated in previous works [34–40]. In this study, the oxygen potential prevailing at the flux–weld-pool interface, as represented by the quantity of FeO in the slag, was reduced by adding aluminium powder. In the same type of reaction as reaction G in Figure 7, namely reduction of MnO from the molten flux by reaction with aluminium, the FeO formed from excess oxygen in the weld pool may also be reduced by aluminium; see reaction (4) in the text. These aluminium-based reduction reactions, as displayed in Equations (2)–(4) in the text, are exothermic and therefore release chemical energy into the weld pool in the form of

heat. This effect was quantified in Section 3.2 above. The extra added heat can be used to melt and dissolve cobalt metal powder into the weld pool.

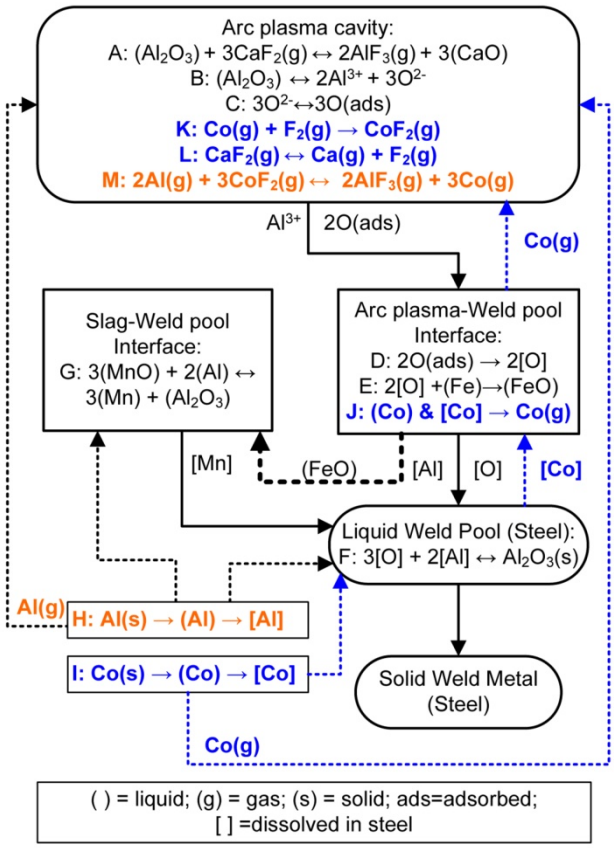

Figure 7. SAW reaction flow diagram with Al and Co powder additions.

The reduced oxygen potential at the flux–weld-pool interface prevented oxidation of cobalt powder to CoO, and so prevented loss of cobalt into the slag. Instead, the cobalt powder melted and dissolved into the weld pool; see reaction I. Since there an excess of Al was added, some of the Al also dissolved into the weld pool; see reaction H. Based on the Gibbs free energy values displayed in Figures 4 and 5 it appears that cobalt loss in SAW with metal powder alloying occured due to cobalt vaporisation and/or subsequent reaction of cobalt vapour with fluorine gas to form CoF_2(g), and reaction of CoF_2(g) with aluminium vapour according to the reaction displayed in Equation (11). This reaction sequence is marked in Figure 7 in blue text, as reactions J, K, and L, and in orange text for reaction with aluminium vapour, reaction M. Cobalt can be vapourised at the arc-plasma–weld-pool interface from the weld pool and from the unconstrained cobalt powder, before it is dissolved into the weld pool. This conclusion is confirmed from the FactSage Equilib gas–slag–metal powder calculations summarised in Table 7. Formation of F_2(g) from the dissociation of CaF_2(g) in the arc plasma appears possible, since the Ca and F were analysed in the arc cavity gas phase when a CaF_2-based flux was used in SAW [1,41]. The added aluminium powder played a role in gas phase reactions by shifting cobalt to vapour instead of oxidation to CoO, as discussed in the above thermodynamic analysis. However, the final arbiter of the oxidation state of cobalt is the partial oxygen pressure at the flux–weld-pool interface, because the final influencing reactions takes place at this interface as the weld pool cools from the high arc plasma temperatures to its solidus temperature.

The results presented here confirm that the oxygen potential at the molten flux–weld interface is lowered by the addition of aluminium powder and this effect plays a critical role in the transfer of cobalt into the weld pool, without interfering with oxygen transfer from the plasma arc to the weld pool. The thermodynamic analysis shows that the likely

chemical reaction of cobalt loss is due to reaction of cobalt vapour with F2(g) to form CoF2(g) in the arc cavity, and not due to for-mation of CoO as intermediate. Furthermore, CoF_2(g) in the arc cavity may easily be transformed to cobalt vapour via reaction (11). The main chemical interaction between cobalt and aluminium occured indirectly via the reduced oxygen potential at the molten flux–weld-pool interface, maintaining cobalt in the metallic form and limiting oxidation of cobalt in the weld pool to CoO, so preventing CoO loss into slag.

5. Conclusions

1. The application of unconstrained cobalt and aluminium powders in SAW was used to alloy carbon steel weld metal to 5.3% Co and 4.2% Al. These alloying numbers were translated by mass balance to calculate yield numbers to the weld metal of 70% for Co and 55% for Al.
2. Sufficient control of the oxygen potential at the slag–weld pool interface was achieved by the application of aluminium powder. This was done without interfering with oxygen transfer from the arc plasma to the weld pool. The total weld metal oxygen content was controlled to 230 ppm O in MP7 weld metal vs. 499 ppm O in the base case wled metal when no metal powder was added.
3. Gas–slag–metal powder equilibrium calculations show that increased Co vapour formation is favoured by increased addition of Al powder to the reaction system, because aluminium fluorides are thermodynamically favoured ahead of CoF_2(g) at the high temperatures in the arc cavity (2500 °C).
4. The application of unconstrained metal powders in SAW improves the overall welding process productivity. Expensive time-consuming steps, namely manufacturing of alloyed wire and alloyed powder, can be eliminated if unconstrained metal powders are applied directly in the SAW process.

Author Contributions: F.D.B. conceptualised the work; F.D.B. and T.C. executed the experiments, interpreted the data, and prepared the manuscript. All authors have read and agreed to the published version of the manuscript.

Funding: This research was funded in part by the National Research Foundation of South Africa, grant number BRIC171211293679.

Data Availability Statement: The data sets presented in this study are available upon request to the corresponding author.

Conflicts of Interest: The authors declare no conflict of interest. The funders had no role in the design of the study; in the collection, analysis, or interpretation of data; in the writing of the manuscript, or in the decision to publish the results.

References

1. Sengupta, V.; Havrylov, D.; Mendex, P.F. Physical phenomena in the weld zone of submerged arc welding—A Review. *Weld. J.* **2019**, *98*, 283–313.
2. O'Brien, A. *Welding Handbook—Materials and Applications, Part 1*, 9th ed.; American Welding Society (AWS): Miami, FL, USA, 2011; Volume 4.
3. Dallam, C.B.; Liu, S.; Olson, D.L. Flux composition dependence of microstructure and toughness of submerged arc HSLA weldments. *Weld. J.* **1985**, *64*, 140–152.
4. Polar, A.; Indacochea, J.E.; Blander, M. Electrochemically generated oxygen contamination in submerged arc welding. *Weld. J.* **1990**, *69*, 68–74.
5. Lau, T.; Weatherly, G.C.; Mc Lean, A. The sources of oxygen and nitrogen contamination in submerged arc welding using CaO-Al2O3 based fluxes. *Weld. J.* **1985**, *64*, 343–347.
6. Eagar, T.W. Sources of weld metal oxygen contamination during submerged arc welding. *Weld. J.* **1978**, *57*, 76–80.
7. Chai, C.S.; Eagar, T.W. Slag metal reactions in binary CaF_2-metal oxide welding fluxes. *Weld. J.* **1982**, *61*, 229–232.
8. Tuliani, S.S.; Boniszewski, T.; Eaton, N.F. Notch toughness of commercial submerged arc weld metal. *Weld. Met. Fabr.* **1969**, *37*, 327–339.
9. Chai, C.S.; Eagar, T.W. Slag-metal equilibrium during submerged arc welding. *Metall. Trans. B* **1981**, *12*, 539–547. [CrossRef]

10. Mitra, U.; Eagar, T.W. Slag-metal reactions during welding: Part I. Evaluation and reassessment of existing theories. *Metall. Trans. B* **1991**, *22*, 65–71. [CrossRef]
11. Palm, J.H. How fluxes determine the metallurgical properties of Submerged Arc Welds. *Weld. J.* **1972**, *51*, 358–360.
12. Paniagua-Mercado, A.M.; Lopez-Hirata, V.M.; Saucedo Munoz, M.L. Influence of the chemical composition of flux on the microstructure and tensile properties of submerged-arc welds. *J. Mater. Proc. Technol.* **2005**, *169*, 346–351. [CrossRef]
13. Bang, K.; Park, C.; Jung, H.; Lee, J. Effects of flux composition on the element transfer and mechanical properties of weld metal in submerged arc welding. *J. Met. Mater. Int.* **2009**, *15*, 471–477. [CrossRef]
14. Singh, B.; Khan, Z.A.; Siddiquee, A.N. Effect of flux composition on element transfer during Submerged Arc Welding (SAW): A literature review. *Int. J. Curr. Res.* **2013**, *5*, 4181–4186.
15. Coetsee, T.; De Bruin, F. Aluminium Assisted Nickel Alloying in Submerged Arc Welding of Carbon Steel: Application of Unconstrained Metal Powders. *Appl. Sci.* **2022**, *12*, 5392. [CrossRef]
16. Coetsee, T.; De Bruin, F.J. Improved titanium transfer in Submerged Arc Welding of carbon steel through aluminium addition. *Miner. Process. Extr. Metall. Rev.* **2021**, *43*, 771–774. [CrossRef]
17. Coetsee, T.; De Bruin, F.J. Reactions at the molten flux-weld pool interface in submerged arc welding. *High Temp. Mater. Processes.* **2021**, *40*, 421–427. [CrossRef]
18. Coetsee, T.; De Bruin, F. Application of Copper as Stabiliser in Aluminium Assisted Transfer of Titanium in Submerged Arc Welding of Carbon Steel. *Processes* **2021**, *9*, 1763. [CrossRef]
19. Coetsee, T.; De Bruin, F. Chemical Interaction of Cr-Al-Cu Metal Powders in Aluminum-Assisted Transfer of Chromium in Submerged Arc Welding of Carbon Steel. *Processes* **2022**, *10*, 296. [CrossRef]
20. Coetsee, T.; De Bruin, F. Aluminium-Assisted Alloying of Carbon Steel in Submerged Arc Welding: Application of Al-Cr-Ti-Cu Unconstrained Metal Powders. *Processes* **2022**, *10*, 452. [CrossRef]
21. ESAB: Hardfacing & High Alloy Product Selection Guide. Available online: https://www.esabna.com/shared/documents/litdownloads/sto-2102a_stoody_hardfacing-highalloy_catalog_8-15-17.pdf (accessed on 8 July 2022).
22. Hybrid Welding: More Emissions Than with WIG and MIG Welding. Available online: https://safe-welding.com/laser-welding-automated-but-hazardous-for-employees-nonetheless/ (accessed on 8 July 2022).
23. Helis, L.; Toda, Y.; Hara, T.; Miyazaki, H.; Abe, F. Effect of cobalt on the microstructure of tempered martensitic 9Cr steel for ultra-supercritical power plants. *Mater. Sci. Eng. A* **2009**, *510–511*, 88–94. [CrossRef]
24. Jing, H.; Luo, Z.; Xu, L.; Zhao, L.; Han, Y. Low cycle fatigue behavior and microstructure of a novel 9Cr-3W-3Co tempered martensitic steel at 650 °C. *Mater. Sci. Eng. A* **2018**, *731*, 394–402. [CrossRef]
25. Hallén, H.; Johansson, K.-E. Use of a Metal Powder for surface coating by Submerged Arc Welding. U.S. Patent 6331688 B1, 18 December 2001.
26. Daily Metal Price. Available online: https://www.dailymetalprice.com/ (accessed on 11 July 2022).
27. Hercik, T.; Sigmund, M.; Hruby, P. Weldability of cobalt alloys by hybrid methods. *MM Sci. J.* **2021**, *2021*, 4946–4953. [CrossRef]
28. Raabe, D.; Tasan, C.C.; Springer, H.; Bausch, M. From high-entropy alloys to high-entropy steels. *Steel Res. Int.* **2015**, *86*, 1127–1138. [CrossRef]
29. Moon, J.; Ha, H.-Y.; Kim, K.-W.; Park, S.-J.; Lee, T.-H.; Kim, S.-D.; Jang, J.H.; Jo, H.-H.; Hong, H.-U.; Lee, B.H.; et al. A new class of lightweight, stainless steels with ultra-high strength and large ductility. *Sci. Rep.* **2020**, *10*, 12140. [CrossRef]
30. Coetsee, T. Phase chemistry of Submerged Arc Welding (SAW) fluoride based slags. *Mater. Res. Technol.* **2020**, *9*, 9766–9776. [CrossRef]
31. Bale, C.W.; Bélisle, E.; Chartrand, P.; Decterov, S.; Eriksson, G.; Gheribi, A.E.; Hack, K.; Jung, I.-H.; Kang, Y.-B.; Melançon, J.; et al. Reprint of: FactSage thermochemical software and databases, 2010–2016. *Calphad* **2016**, *55*, 1–19. [CrossRef]
32. Kluken, A.O.; Grong, Ø. Mechanisms of inclusion formation in Al-Ti-Si-Mn deoxidized steel weld metals. *Metall. Trans. B* **1989**, *20*, 1335–1349. [CrossRef]
33. Mitra, U.; Eagar, T.W. Slag-metal reactions during welding: Part II. Theory. *Metall. Trans. B* **1991**, *22*, 73–81. [CrossRef]
34. Mitra, U.; Eagar, T.W. Slag metal reactions during submerged arc welding of alloy steels. *Metall. Trans. B* **1984**, *15*, 217–227. [CrossRef]
35. Zhang, J.; Coetsee, T.; Basu, S.; Wang, C. Impact of gas formation on the transfer of Ti and O from TiO_2-bearing basic fluoride fluxes to submerged arc welded metals: A thermodynamic approach. *Calphad* **2020**, *71*, 102195. [CrossRef]
36. Coetsee, T.; Mostert, R.J.; Pistorius, P.G.H.; Pistorius, P.C. The effect of flux chemistry on element transfer in Submerged Arc Welding: Application of thermochemical modelling. *Mater. Res. Technol.* **2021**, *11*, 2021–2036. [CrossRef]
37. Zhang, J.; Coetsee, T.; Wang, C. Element transfer behaviors of fused CaF_2-SiO_2 fluxes subject to high heat input submerged arc welding. *Metall. Trans. B* **2020**, *51*, 16–21. [CrossRef]
38. Zhang, J.; Coetsee, T.; Dong, H.; Wang, C. Element transfer behaviors of fused CaF_2-SiO_2-MnO fluxes under high heat input submerged arc welding. *Metall. Trans. B* **2020**, *51*, 885–890. [CrossRef]
39. Zhang, J.; Coetsee, T.; Dong, H.; Wang, C. Element transfer behaviors of fused CaF_2-TiO_2 fluxes in EH36 shipbuilding steel during high heat input Submerged Arc Welding. *Metall. Trans. B* **2020**, *51*, 1953–1957. [CrossRef]

40. Coetsee, T.; De Bruin, F. In Situ Modification of CaF_2-SiO_2-Al_2O_3-MgO Flux Applied in the Aluminium-Assisted Transfer of Titanium in the Submerged Arc Welding of Carbon Steel: Process Mineralogy and Thermochemical Analysis. *Minerals* **2022**, *12*, 604. [CrossRef]
41. Gött, G.; Gericke, A.; Henkel, K.-M.; Uhrlandt, D. Optical and spectroscopic study of a submerged arc welding cavern. *Weld. J.* **2016**, *95*, 491–499.